Coordinated autoinhibition of F-BAR domain membrane binding and WASp activation by Nervous Wreck

Tatiana B. Stanishneva-Konovalova[a,1], Charlotte F. Kelley[b,1], Tania L. Eskin[b], Emily M. Messelaar[b], Steven A. Wasserman[b], Olga S. Sokolova[a,2], and Avital A. Rodal[b,2]

[a]Department of Bioengineering, Faculty of Biology, M.V. Lomonosov Moscow State University, 119234 Moscow, Russia; and [b]Rosenstiel Basic Medical Sciences Research Center, Department of Biology, Brandeis University, Waltham, MA 02453

Edited by Gregory A. Petsko, Weill Cornell Medical College, New York, NY, and approved July 25, 2016 (received for review December 10, 2015)

Membrane remodeling by Fes/Cip4 homology-Bin/Amphiphysin/Rvs167 (F-BAR) proteins is regulated by autoinhibitory interactions between their SRC homology 3 (SH3) and F-BAR domains. The structural basis of autoregulation, and whether it affects interactions of SH3 domains with other cellular ligands, remain unclear. Here we used single-particle electron microscopy to determine the structure of the F-BAR protein Nervous Wreck (Nwk) in both soluble and membrane-bound states. On membrane binding, Nwk SH3 domains do not completely dissociate from the F-BAR dimer, but instead shift from its concave surface to positions on either side of the dimer. Unexpectedly, along with controlling membrane binding, these autoregulatory interactions inhibit the ability of Nwk-SH3a to activate Wiskott–Aldrich syndrome protein (WASp)/actin related protein (Arp) 2/3-dependent actin filament assembly. In *Drosophila* neurons, Nwk autoregulation restricts SH3a domain-dependent synaptopod formation, synaptic growth, and actin organization. Our results define structural rearrangements in Nwk that control F-BAR–membrane interactions as well as SH3 domain activities, and suggest that these two functions are tightly coordinated in vitro and in vivo.

F-BAR | actin | *Drosophila* | Nwk | WASp

Eukaryotic membranes are shaped and remodeled by a host of lipid-binding proteins that must be highly regulated to enable the rapid dynamics of cell morphogenesis and intracellular traffic. Members of the Bin/Amphiphysin/Rvs167 (BAR) family of proteins dimerize to form a crescent-shaped membrane-interacting scaffold that can stabilize or generate membrane curvature (1). It remains poorly understood how these scaffolds are targeted to specific membranes in vivo, and how their activities are regulated to direct membrane dynamics in diverse contexts.

Many BAR family members contain C-terminal SRC homology 3 (SH3) domains that interact with proline-rich ligands, including dynamin, a large GTPase that promotes membrane scission, and Wiskott–Aldrich syndrome protein (WASp), which promotes actin filament assembly via the actin-related protein (Arp) 2/3 complex (2–5). WASp itself is autoregulated by inhibitory interactions between its N terminus and its C-terminal Arp2/3-activating verprolin-central-acidic (VCA) domain, and can be activated by the combined effects of SH3 domain-containing binding partners, charged phospholipids, Rho family GTPases, and induced multimerization (6). For several BAR family members, including Syndapin, Amphiphysin, and Nervous Wreck (Nwk), C-terminal SH3 domains also bind directly to the BAR domain, inhibiting membrane association (7–16).

Mounting evidence suggests that ligands of the BAR and/or SH3 domains may release this autoinhibition, providing regulatory inputs into membrane remodeling in vivo (8, 9, 12); however, little is known about the structural basis of autoinhibition in BAR domain proteins, or its effect on their interactions with binding partners. This raises the possibility that autoinhibition in solution affects the activities of SH3 domains on ligands such as WASp and dynamin. Furthermore, once the BAR domain is bound to the membrane, it is unclear whether the adjacent SH3 domains function independently or instead remain influenced by their proximity to the BAR domain.

Drosophila Nervous Wreck is a neuronal F-BAR (Fes/Cip4-homology-BAR) domain protein with two C-terminal SH3 domains (Fig. 1*A*). The Nwk F-BAR domain forms a dimer that assembles into higher-order zigzag arrays on negatively charged membranes and promotes the formation of membrane ridges and scallops (17). Nwk is required at the *Drosophila* larval neuromuscular junction (NMJ) to constrain the traffic and signaling activity of growth factor receptors (18–20). Mammalian genomes encode two Nwk family members, FCHSD1 and FCHSD2, which are associated with stereocilia and the trafficking of neurotransmitter receptors (21, 22). Nwk interacts with WASp and dynamin via its SH3a domain (19, 20), and cooperates with Cdc42 to activate WASp/Arp2/3-mediated actin polymerization (20). We previously showed that both SH3 domains of Nwk bind directly to the Nwk F-BAR domain in solution via electrostatic interactions, shifting the lipid charge requirements for Nwk-induced membrane deformation (16). Here we describe the

Significance

Membrane-deforming proteins cooperate with the cytoskeleton to sculpt lipid bilayers into complex and dynamic geometries, but we still do not understand how their activities are temporally and spatially regulated in cells. Here we show that the neuronal membrane remodeling protein Nervous Wreck (Nwk) is autoinhibited by intramolecular interactions between its membrane binding F-BAR domain and its C-terminal SRC homology 3 (SH3) domains. These autoinhibitory interactions control Fes/Cip4 homology-Bin/Amphiphysin/Rvs167 (F-BAR)–mediated membrane remodeling and also, unexpectedly, inhibit SH3-mediated actin cytoskeleton assembly. Uncoupling these dual autoregulatory mechanisms in the fruit fly leads to excess neuronal synapse growth. Thus, coordinated autoregulation couples membrane remodeling and SH3 domain activities, and is critical for proper control of neuronal shape and size.

Author contributions: T.B.S.-K., C.F.K., O.S.S., and A.A.R. designed research; T.B.S.-K., C.F.K., T.L.E., E.M.M., S.A.W., O.S.S., and A.A.R. performed research; C.F.K., O.S.S., and A.A.R. contributed new reagents/analytic tools; T.B.S.-K., C.F.K., T.L.E., E.M.M., S.A.W., O.S.S., and A.A.R. analyzed data; and C.F.K., O.S.S., and A.A.R. wrote the paper.

The authors declare no conflict of interest.

This article is a PNAS Direct Submission.

Data deposition: Electron microscopy data have been deposited in EMDataBank (entry nos. EMD-8161 and EMD-8156).

[1]T.B.S.-K. and C.F.K. contributed equally to this work.

[2]To whom correspondence may be addressed. Email: sokolova184@gmail.com or arodal@brandeis.edu.

This article contains supporting information online at www.pnas.org/lookup/suppl/doi:10.1073/pnas.1524412113/-/DCSupplemental.

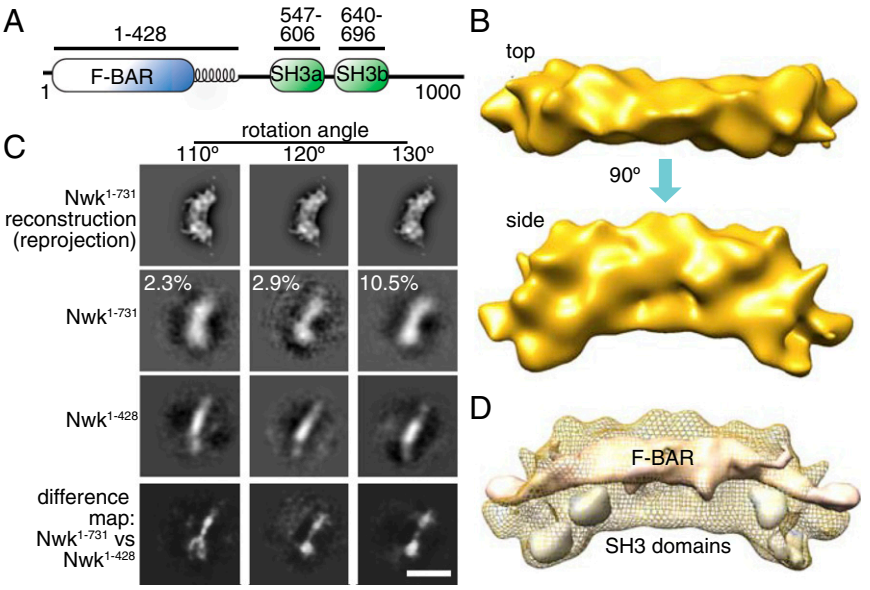

Fig. 1. Structure of non–membrane-bound Nwk. (*A*) Domain structure of Nwk. (*B*) 3D reconstruction of Nwk$^{1–731}$ dimers on carbon film, viewed from above the convex surface (top) or rotated along its long axis by 90° (side). (*C*) Side-lying reprojections of the Nwk$^{1–731}$ 3D reconstruction (first row); matching 2D class averages of Nwk$^{1–731}$, identified by projection matching to the 3D reconstruction (second row); Nwk$^{1–428}$ on carbon film, identified by projection mapping to a homology model of Nwk$^{1–313}$ (17) (third row); and difference maps (fourth row). White regions in the difference maps show additional density in Nwk$^{1–731}$, below the black regions representing the central F-BAR mass. Numbers indicate the percentage of total particles represented in the class. (*D*) Model of position of Nwk SH3 domains in 3D reconstruction. Predicted structures of Nwk$^{1–313}$ (pink) and the SH3b domain of Nwk [gray, used to model both SH3a and SH3b (16)] were filtered to 20 Å and fitted into the reconstruction of Nwk$^{1–731}$. The Nwk$^{1–313}$ homology model, based on FBP17 (17), was not used for calculating 3D reconstructions and is shown here for comparative purposes only. (Scale bar: 20 nm.)

effects of autoregulation on SH3 domain function on membranes, in solution, and in vivo.

Results

Structure of Non–Membrane-Bound Nwk. To address how autoregulatory interactions affect F-BAR protein activity and function, we used negative-stain electron microscopy (EM) and single-particle analysis to determine the structure of Nwk (purified proteins shown in Fig. S1 *A–D*). Nwk$^{1–731}$ is an autoinhibited Nwk construct that includes all of its major domains (Fig. 1*A*) and rescues function in vivo (16, 23). We first analyzed Nwk$^{1–731}$ in the absence of membranes, on carbon-coated grids (Fig. S2 *A–D*). Single-particle class averages exhibited symmetry (Fig. S3*A*), and particles were randomly oriented on the grid (Fig. S3*B*), allowing us to use the angular reconstitution method (24) to generate a 3D reconstruction (Fig. 1*B* and Fig. S3 *C* and *D*). For this reconstruction, we excluded class averages (16% of total particles) that were similar to those of the F-BAR domain alone. These are likely to represent the fraction in equilibrium of "open" Nwk$^{1–731}$, in which the F-BAR is available for membrane binding (16, 17) and SH3 domain positions are not constrained (and thus are not defined in class averages). Compared with the isolated F-BAR domain (Nwk$^{1–428}$), which forms an S-shaped dimer (17), our Nwk$^{1–731}$ 3D reconstruction exhibited an overall arrangement consistent with an F-BAR domain-shaped mass with additional masses positioned below its concave surface (Fig. 1*B*).

To determine the positions of the C-terminal SH3 domains within this reconstruction, we used an unbiased approach to identify side-lying Nwk$^{1–731}$ and Nwk$^{1–428}$ class averages (*Materials and Methods*). When we compared these class averages with each other, the additional mass in Nwk$^{1–731}$ was present adjacent to the concave surface of the F-BAR (Fig. 1*C*). These data indicate that in autoinhibited Nwk, the F-BAR concave surface is largely blocked by the C-terminal SH3 domains (model, Fig. 1*D*).

Structure of Membrane-Bound Nwk. We next used negative-stain EM and single-particle analysis to examine the structure and higher-order organization of Nwk on PI(4,5)P_2-containing membrane monolayers (Fig. S4 *A–D*). We first determined the orientation of 2D class averages for Nwk$^{1–731}$ dimers on carbon film vs. membrane monolayers (Fig. S5*A*, Table S1, and *Materials and Methods*). Compared with membrane-free Nwk, membrane monolayer-associated Nwk$^{1–731}$ was biased toward orientations in which the concave surface faced the membrane, consistent with a conventional F-BAR–membrane association (25). We next examined the higher-order organization of Nwk$^{1–731}$ on membrane monolayers. Nwk$^{1–731}$ oligomerized in V-shape dimer pairs and zigzags (Fig. S5 *B* and *C*), similar to the arrangements of Nwk$^{1–428}$ alone (17). Therefore, Nwk$^{1–731}$ associates with membranes in a similar fashion to Nwk$^{1–428}$, consistent with their similar membrane remodeling activities (16, 17).

Because the Nwk$^{1–731}$ single-particle class averages exhibited symmetry (Fig. S6*A*) and particles showed a preferred orientation on the membrane (Fig. S6*B*), we were able to produce a 3D reconstruction using the random conical tilt method (Fig. 2*A* and Fig. S6 *C* and *D*). For this reconstruction, we used 80.7% of the total particles, representing the concave-down or side-down orientations (see above) that we previously showed to be favored for higher-order assembly and for membrane binding (16, 17). In contrast to the S-shape of Nwk$^{1–428}$ on membranes (17) and the vertical arrangement of the F-BAR domain above the SH3 domains for Nwk$^{1–731}$ on carbon film (Fig. 1 *B* and *D*), the membrane-bound Nwk$^{1–731}$ dimers displayed a flattened dumbbell shape (Fig. 2*A* and Fig. S6*D*). Compared with the predicted structure of Nwk$^{1–313}$ filtered to 20 Å (Fig. 2*B*, pink) (17), the reconstruction revealed a mass on the inner surface of the curve of the S-shaped dimer (Fig. 2*B*, red arrows), along with a mass on the outside surface of the curve (Fig. 2*B*, blue arrows), as well as an additional mass near the center of the F-BAR domain (Fig. 2*B*, green arrows). Interestingly, these masses did not occlude the F-BAR tips, consistent with our results showing that the tips are required for efficient membrane binding (17).

To determine which of the additional masses represents each Nwk SH3 domain, we analyzed monolayer-bound single-particle averages of truncated Nwk proteins lacking one or both SH3 domains (Fig. 2 *C* and *D*). Subtracting the Nwk$^{1–428}$ concave side-down class average from the Nwk$^{1–633}$ class averages (lacking SH3b) revealed a mass on the inner curve of the S-shaped F-BAR (Fig. 2*D*). In contrast, subtracting Nwk$^{1–633}$ class averages from Nwk$^{1–731}$ class averages revealed a mass on the outer curve of the S-shaped F-BAR (Fig. 2*C*). Thus, we conclude that the small mass on the inner curve is SH3a, and the mass on the outer curve is SH3b (models, Fig. 2 *C* and *D*). Importantly, our 3D model indicated that on average, the SH3 domains were not disordered in the membrane-bound structure, but instead were associated with the F-BAR domain at specific positions. This is somewhat surprising, given the

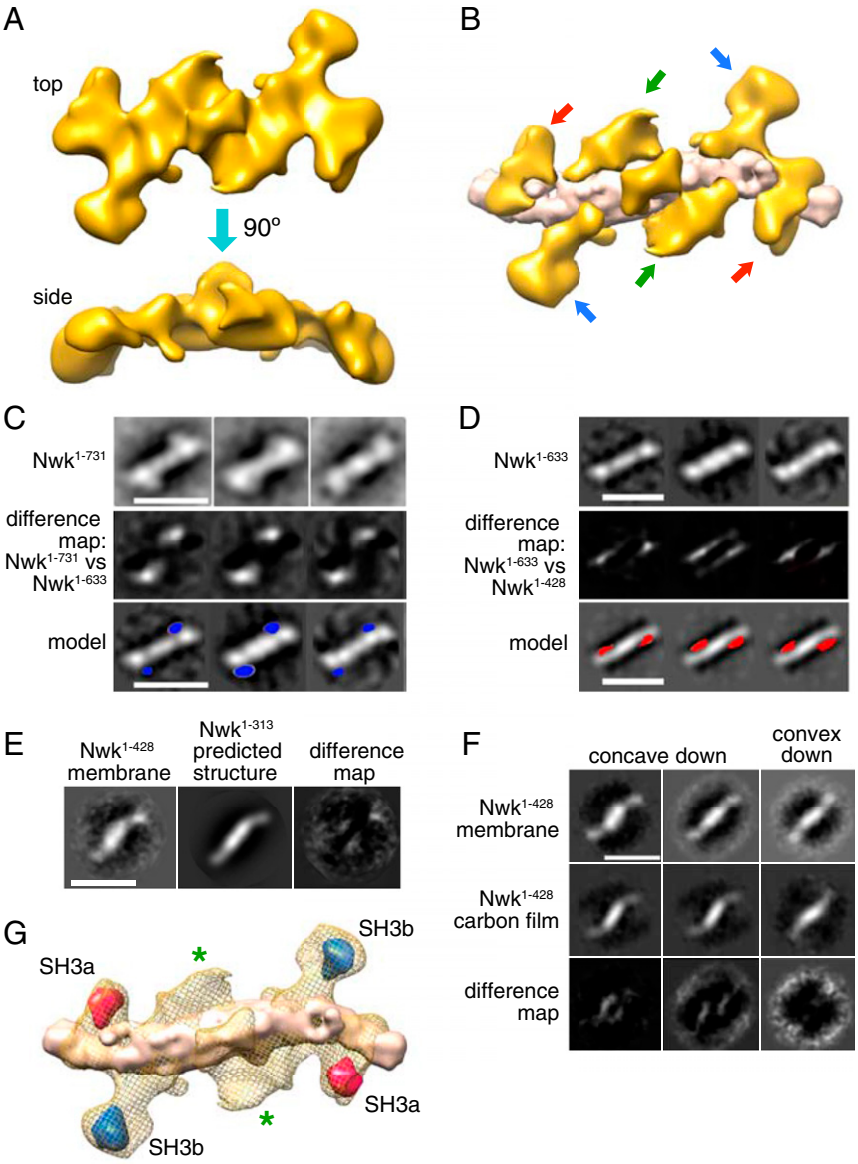

Fig. 2. Structure of membrane-bound Nwk. (*A*) 3D reconstruction of Nwk$^{1–731}$ on membrane monolayers (molar percentages of PC/PE/PS/PI(4,5)P2: 65/15/10/10, with <0.1% rhodamine-PE for visualization) viewed from above the convex surface (top) or rotated along its long axis by 90° (side). (*B*) The predicted structure of Nwk$^{1–313}$ (pink) (17) was filtered to 20 Å and fitted into the reconstruction of Nwk$^{1–731}$. The Nwk$^{1–313}$ homology model, based on FBP17 (17), was not used for calculating 3D reconstructions and is shown here for comparative purposes only. Arrows indicate masses in Nwk$^{1–731}$ that are absent in Nwk$^{1–313}$. Red arrows indicate mass on the inner curve of the S-shaped dimer, blue arrows indicate mass on the outer curve of the S-shaped dimer, and the green arrow indicates mass adjacent to the center of the F-BAR dimer. (*C*) Three class averages of Nwk$^{1–633}$ on lipid monolayers (*Top*), difference map between Nwk$^{1–428}$ and Nwk$^{1–633}$ (*Middle*; white regions show density absent in the Nwk$^{1–428}$ structure) and model of the position of SH3a (*Bottom*). (*D*) Three class averages of Nwk$^{1–731}$ on lipid monolayers (*Top*), difference map between Nwk$^{1–633}$ and Nwk$^{1–731}$ (*Middle*; white regions show density absent in the Nwk$^{1–633}$ structure), and model of the position of SH3b (*Bottom*). (*E*) 2D class average and difference map between Nwk$^{1–428}$ on membrane monolayers (16) and the Nwk$^{1–313}$ homology model (concave surface down; 160° rotation relative to concave surface up). (*F*) 2D class averages of Nwk$^{1–428}$ on carbon film, and difference map between Nwk$^{1–428}$ on membrane monolayers and Nwk$^{1–428}$ on carbon. White regions show shifted density on membrane binding. The central mass corresponding to the alpha-helical extension is displaced laterally in the concave surface-down membrane-bound structure. (*G*) Model of the positions of the Nwk SH3 domains in 3D reconstruction. The green asterisk indicates the proposed position of F-BAR alpha-helical extension Nwk$^{292–428}$. All EM images represent views from above the plane of the membrane. (Scale bars: 20 nm.)

prevailing hypothesis that on membrane binding, the SH3 domains are unleashed and available to interact with their ligands.

We next sought to identify the additional mass that appears in membrane-bound Nwk$^{1–731}$, located in the same plane as the F-BAR dimer and concentrated near its center (Fig. 2*B*, green arrows). This mass also could be seen after subtracting the predicted structure of Nwk$^{1–313}$ from our previously determined structure of Nwk$^{1–428}$ on membranes with its concave surface down (17) (Fig. 2*E*), suggesting that it represents the 115-aa alpha-helical stretch that is C-terminal to the F-BAR domain. Interestingly, this mass was missing in the plane of the F-BAR domain in the carbon film Nwk$^{1–731}$ structure (Fig. 1 *B* and *D*), as well as in single-particle class averages of Nwk$^{1–428}$ either on carbon or oriented with its concave surface up on membrane monolayers (Fig. 2*F*). These results suggest that on membrane binding, both the alpha-helical extension and the SH3 domains shift their position relative to the F-BAR domain, switching from occluding the concave surface to a position adjacent to the F-BAR domain (Fig. 2*G*).

Roles of Nwk SH3 and F-BAR Domains in WASp Activation in Solution. The role of autoinhibitory SH3 domains in regulating F-BAR membrane binding is well established (8, 9, 16); however, our structural data showing SH3-F-BAR associations raise the converse question of how these intramolecular interactions affect SH3 regulation of other cellular factors. We previously identified Nwk$^{1–731}$ as a modest activator of Arp2/3-dependent actin polymerization by binding to and partly relieving autoinhibition of WASp (23). In that study, mutation of the core tryptophan in the Nwk SH3a domain abolished WASp binding and activation, and the core tryptophan in the Nwk SH3b domain was required for a counteracting weak negative effect on WASp activation (23). Here we further explored the role of F-BAR–SH3 interactions in WASp-Arp2/3–mediated actin assembly using an autoinhibited fragment of WASp (WASp$^{\Delta 143}$, lacking its EVH1 domain; ref. 23) and pyrene-actin assembly assays.

Strikingly, both the Nwk SH3a domain (Nwk$^{536–601}$) and the F-BAR+SH3a domain (Nwk$^{1–633}$) were much more potent activators of WASp than Nwk$^{1–731}$, which contains both SH3 domains (Fig. 3 *A* and *B*). Nwk may activate WASp through a combination of SH3 domain-mediated release from the autoinhibited conformation of WASp and F-BAR–induced dimerization of WASp (26). Indeed, quantification of these effects showed that dimerization of the SH3a domain via a GST tag increased its potency to the level of Nwk$^{1–633}$ (Fig. 3*C*). These results suggest that

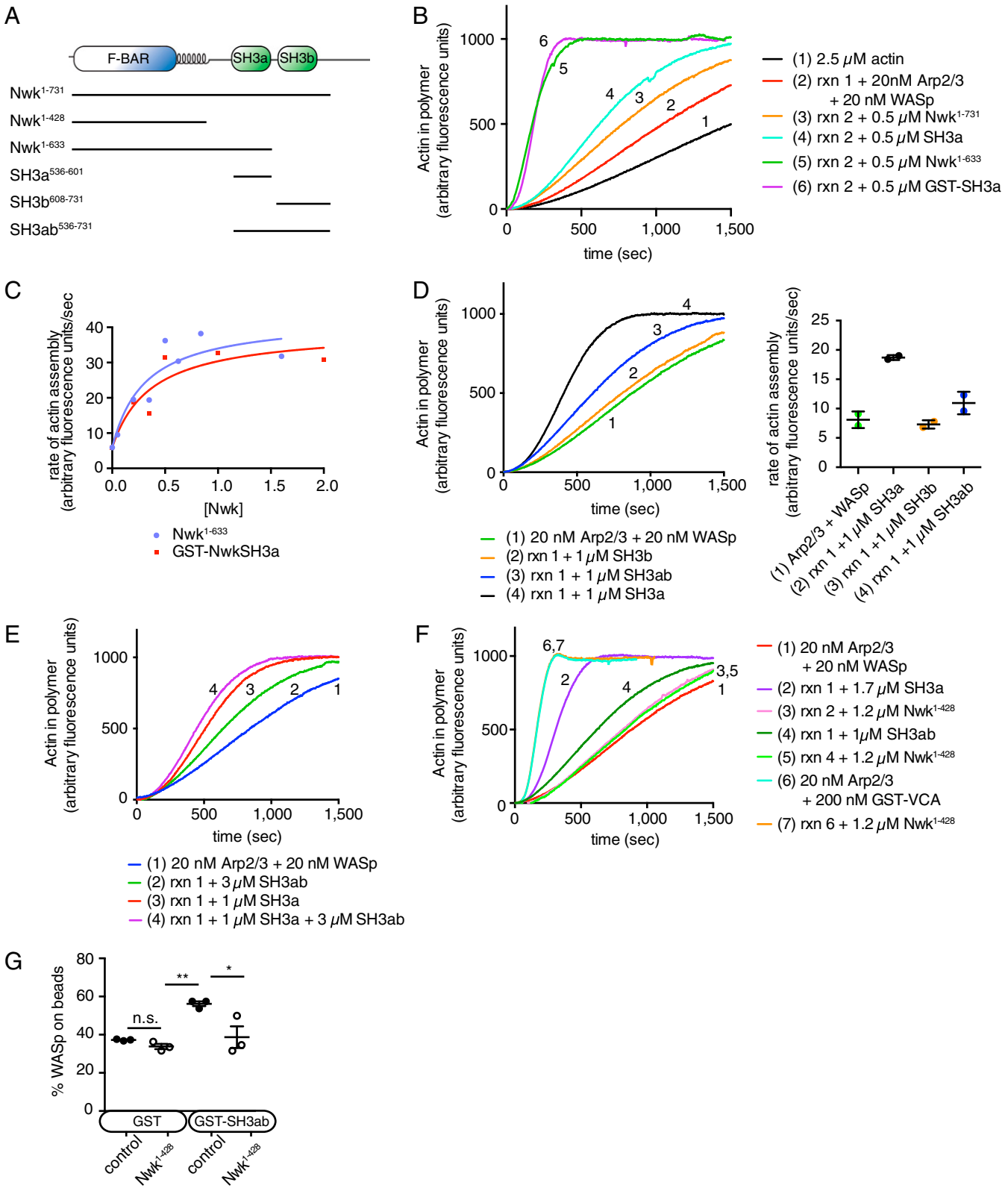

Fig. 3. Roles of Nwk SH3 and F-BAR domains in WASp activation in solution. (*A*) Schematic of protein fragments. (*B–F*) Actin [2.5 μM, 5% (mol/mol) pyrene-labeled] was polymerized in the presence of the indicated proteins. (*B*) Nwk$^{1–731}$ is autoinhibited, and the Nwk SH3a domain promotes WASp-mediated actin assembly. (*C*) Nwk$^{1–633}$ and GST-NwkSH3a have a similar capacity for WASp activation. Rates were calculated from the linear range of pyrene-actin polymerization curves. (*D* and *E*) Role of Nwk SH3 domains in WASp activation. SH3b functions *in cis* to SH3a to suppress WASp activation. The graph shows the mean and range from two independent experiments. (*F*) The Nwk F-BAR domain inhibits its SH3 domain *in trans*. (*G*) The Nwk F-BAR domain competes for WASp binding with Nwk SH3 domains. Here 1 μM GST-SH3ab was incubated with 375 nM WASp and 1.5 μM Nwk$^{1–428}$. Beads were precipitated, and supernatants and pellets were evaluated by immunoblotting. The graph shows the mean ± SEM of three independent reactions. Statistical significance was calculated by ANOVA followed by Tukey's pairwise comparisons.

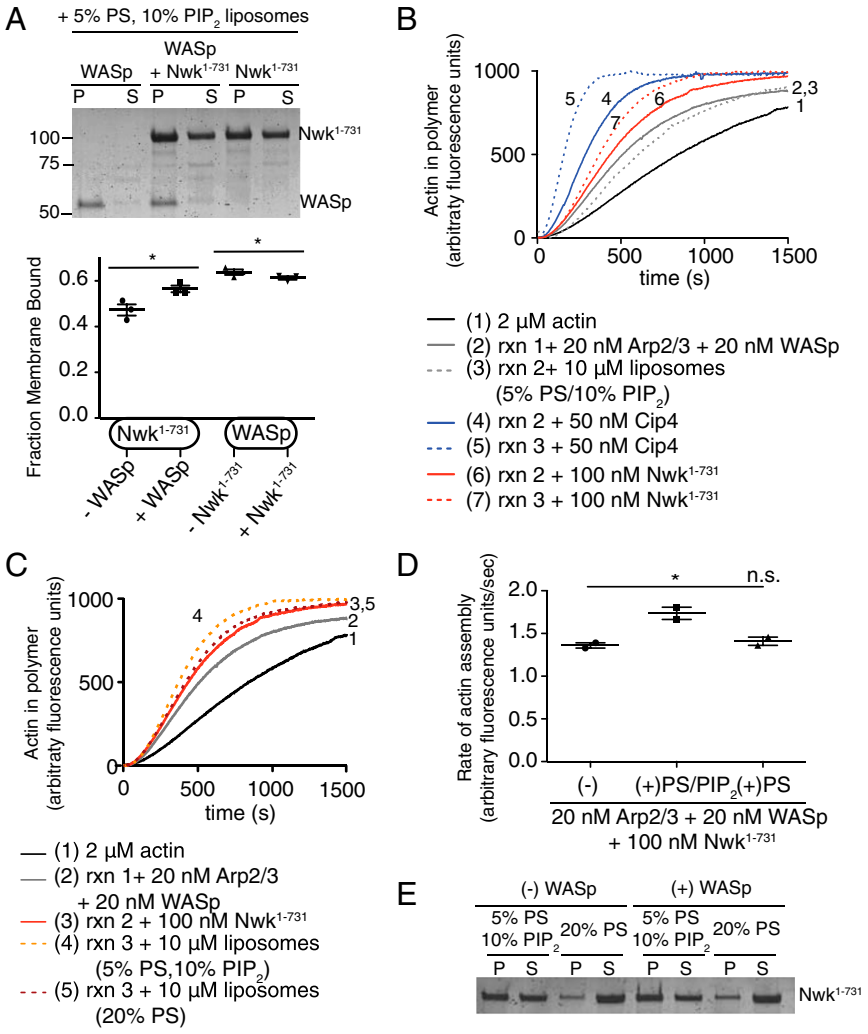

Fig. 4. WASp activation by Nwk is partially stimulated by PI(4,5)P_2 liposomes. (*A*) Purified proteins (0.5 μM WASp, 1 μM Nwk$^{1–731}$) were incubated with liposomes [mol% PC/PE/PS/PI(4,5)P_2: 80/5/5/10] and subjected to liposome cosedimentation assays. The image shows representative Coomassie staining of pellet (P) and supernatant (S) fractions. The graph shows mean ± SEM densitometry from three independent experiments. Statistical significance was calculated for each protein using Student's *t* test. (*B*) Actin [2 μM, 5% (mol/mol) pyrene-labeled] was polymerized in the presence of WASp, Arp2/3, and the indicated F-BAR proteins. WASp activation by both CIP4 and Nwk is enhanced by preincubation with liposomes [mol% PC/PE/PS/PI(4,5)P_2: 80/5/5/10], but not control buffer. Nwk does not activate as strongly as CIP4 in the presence or absence of membrane. (*C*) WASp activation by Nwk is enhanced by PC/PE/PS/PI(4,5)P_2 liposomes, but not by PC/PE/PS (75:5:20) liposomes. (*D*) Rates were calculated from the linear range of pyrene-actin polymerization curves in *C* for two independent experiments. Statistical significance was calculated by ANOVA followed by Tukey's pairwise test. (*E*) Increased actin polymerization corresponds to a higher percentage of membrane-bound Nwk for PC/PE/PS/PI(4,5)P_2 compared with PC/PE/PS liposomes in cosedimentation assays. Nwk membrane binding is similar in the presence or absence of 250 nM WASp for both conditions.

Nwk activates WASp via its SH3a domain, and that dimerization of SH3a (by virtue of its connection to the F-BAR dimer) is important for activity. Furthermore, our data suggest that sequences C-terminal to SH3a negatively impact WASp activation.

To better understand how these C-terminal sequences dampen WASp activation, we tested for inhibitory effects independent of the F-BAR domain. Nwk SH3ab (Nwk$^{536–731}$) showed a reduced ability to stimulate WASp compared with the isolated SH3a domain (Nwk$^{536–601}$) (Fig. 3 *A* and *D*). These results suggest either that SH3b (or flanking sequences) bind to SH3a and/or WASp, or that the presence of SH3b (*in cis*) sterically inhibits SH3a activation of WASp. To help distinguish between these two models, we tested the ability of SH3ab or SH3b (Nwk$^{608–731}$) to affect Nwk-SH3a activity *in trans*. We found that 3 μM Nwk-SH3ab failed to inhibit the stimulatory effects of Nwk-SH3a on WASp (Fig. 3*E*), suggesting that the sequences C-terminal to SH3a obstruct the stimulatory effects of SH3a on WASp only when present in the same molecule.

We next asked whether the Nwk F-BAR domain affects SH3-mediated WASp activation. The Nwk F-BAR (Nwk$^{1–428}$) added *in trans* strongly inhibited the stimulatory effects of both Nwk-SH3a and Nwk-SH3ab on WASp (Fig. 3*F*). Importantly, Nwk$^{1–428}$ had no effect on the Arp2/3 complex activated by WASp GST-VCA domain, indicating that inhibition by Nwk$^{1–428}$ depends on SH3a interactions with regulatory sequences in WASp located outside of its VCA domain (Fig. 3*F*). In contrast to these *in trans* effects, we did not observe autoinhibition when the F-BAR and SH3a domains were present *in cis* in Nwk$^{1–633}$, perhaps owing to steric limitations when these domains are in the same molecule (Fig. 3*B*). Therefore, in the context of the full-length protein, F-BAR–mediated autoinhibition must occur primarily via Nwk SH3b.

We next tested the effects of Nwk$^{1–428}$ on Nwk–SH3ab–WASp interactions, and found that WASp coprecipitation with GST-Nwk-SH3ab was significantly reduced in the presence of excess Nwk F-BAR (Fig. 3*G*). Taken together, these results indicate that in addition to the previously characterized role of F-BAR–SH3 interactions in regulating membrane binding, autoinhibitory interactions between Nwk F-BAR and SH3 domains and *in cis* effects from the SH3b region work together to inhibit SH3a-mediated WASp activation in solution.

Membrane Binding Weakly Activates Nwk for WASp/Arp2/3 Actin Assembly. WASp contains a lipid-binding domain (27, 28), and BAR domain proteins, including Cip4/Toca-1, Syndapin, and Snx9, have been shown to enhance the recruitment of WASp to membranes and to stimulate WASp-Arp2/3–mediated actin assembly (29–31). To examine whether Nwk has similar effects, we performed liposome cosedimentation assays using Nwk and WASp. The binding of Nwk$^{1–731}$ to charged PC/PE/PS/PI(4,5)P_2 liposomes increased slightly in the presence of WASp, whereas WASp binding to liposomes decreased slightly in the presence of Nwk$^{1–731}$ (Fig. 4*A*). Based on the modest levels of these effects, we conclude that Nwk and WASp together do not have dramatically different membrane-binding properties than those of either protein alone.

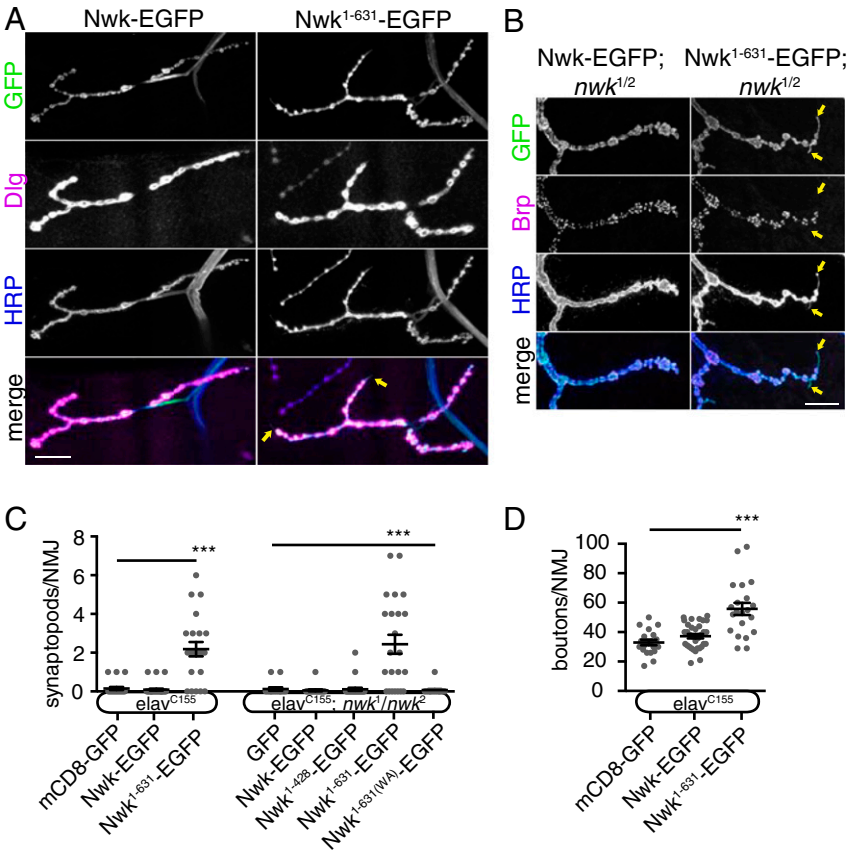

Fig. 5. Nwk autoinhibition restricts SH3a-dependent synaptopod formation. (*A*) Nwk$^{1-631}$ generates synaptopods and increases synaptic growth. Images show representative maximum intensity projections of confocal Z-stacks of NMJs on muscle 4, segments A2-A3. Yellow arrows indicate synaptopods. (Scale bar: 20 μM.) (*B*) Localization of Nwk variants. Images show representative maximum intensity projections of laser scanning confocal images. Arrows indicate synaptopods. (Scale bar: 10 μM.) (*C* and *D*) Quantification of synaptopods and synaptic growth on muscle 4, segments A2-A3. n represents the number of NMJs measured. WT background genotypes are elav^{C155}/+ or Y; UAS/+; *nwk* mutant background genotypes are elav^{C155}/+ or Y; UAS/+; *nwk*^{1}/*nwk*^{2}. WT background: UAS-CD8-GFP n = 20 NMJs; UAS-Nwk^{FL}-GFP n = 33 NMJs; UAS-Nwk$^{1-631}$-GFP n = 21 NMJs; *nwk* mutant background: UAS-GFP n = 16 NMJs; UAS-Nwk^{FL}-GFP n = 20 NMJs; UAS-Nwk$^{1-428}$-GFP n = 23 NMJs; UAS-Nwk$^{1-631}$-GFP n = 33 NMJs; UAS-Nwk$^{1-631\text{-}W581A}$-GFP n = 16 NMJs. Graphs show mean ± SEM. Statistical significance was calculated by ANOVA followed by Tukey's pairwise test.

We next tested the effects of charged liposomes on Nwk activation of WASp/Arp2/3-mediated actin assembly. Activation of WASp by *Drosophila* Cip4 was potentiated by PI(4,5)P_2-containing membranes, whereas Nwk$^{1-731}$ activation of WASp was only modestly stimulated by PI(4,5)P_2-containing membranes under these conditions (Fig. 4 *B* and *C*). In contrast, weakly negatively charged liposomes lacking PI(4,5)P_2 bound poorly to Nwk$^{1-731}$ and failed to enhance Nwk$^{1-731}$–dependent WASp activation (Fig. 4 *C*–*E*). These results suggest that PI(4,5)P_2-dependent lipid binding modestly enhances the ability of Nwk to activate WASp, but that significant autoinhibition persists on the membrane.

Consequences of Misregulated Nwk-Induced Actin Assembly in Vivo. We next tested the consequences of misregulated Nwk in vivo, at the *Drosophila* larval NMJ. At NMJ axon terminals, Nwk localizes to an endocytically active region called the "periactive zone," adjacent to sites of neurotransmitter release (18). *nwk* mutants exhibit overgrowth of the NMJ, likely owing to a failure to downregulate synaptic growth signaling by Bone Morphogenic Protein (BMP) receptors (19, 23). We previously showed that the F-BAR domain of Nwk is required for its localization to periactive zones and its ability to restrict synaptic growth; however, the F-BAR domain alone localized aberrantly to the plasma membrane and caused an even more severe synaptic growth phenotype than the null mutant, suggesting that unregulated membrane binding is deleterious (16). Here, to test the role of autoregulation in Nwk-induced actin assembly in vivo, we used the binary GAL4/UAS system to pan-neuronally express Nwk$^{1-631}$, analogous to the Nwk fragment that exhibits unregulated actin assembly (Fig. 3 *A* and *B*) and partially deregulated membrane binding (16) in vitro, tagged at its C terminus with GFP. Unexpectedly, Nwk$^{1-631}$-GFP–expressing NMJs exhibited long, thin protrusions, frequently extending from the terminal bouton of the NMJ but sometimes emanating from boutons more proximal to the entry point of the nerve into the muscle (Fig. 5*A*, yellow arrows). Nwk$^{1-631}$-GFP localized throughout the boutons in a reticular pattern similar to wild type (WT) Nwk-GFP, and extended into the protrusions (Fig. 5*B*). The protrusions contained the neuronal membrane marker that is recognized by α-HRP antibodies but did not contain active zones, recognized by α-Bruchpilot (Brp) antibodies, or postsynaptic specializations, recognized by α-Discs Large (Dlg) antibodies. This phenotype was present for Nwk$^{1-631}$ expressed in both WT and *nwk* mutant backgrounds and, importantly, was not seen in *nwk* null larvae or in larvae overexpressing WT Nwk-GFP, Nwk$^{1-428}$-GFP, or Nwk$^{1-631}$ with an SH3a point mutation (W581A) that abolishes interactions with proline-rich ligands (23) (Fig. 6*C*). This phenotype has not been previously associated with Nwk, but has been observed at early stages of activity-dependent synaptic growth (32, 33), as well as in mutants of the cytoskeletal protein Hts/Adducin (34). These structures, known as synaptopods, are thought to mature into "ghost boutons" with active zones but no postsynaptic specialization and to ultimately develop into mature boutons (32, 33). In fact, occasional faint accumulations of Dlg could be seen in some Nwk$^{1-631}$-dependent synaptopods (Fig. 5*A*), and Nwk$^{1-631}$-expressing animals showed a significant increase in total boutons (Fig. 5*D*), suggesting that synaptopods are bouton precursors. These results indicate that synaptopod formation is a gain-of function phenotype resulting from deregulated Nwk$^{1-631}$, and depends on the ability of the SH3a domain-containing region to interact with proline-rich ligands.

To ask whether the morphological defects arising from deregulated Nwk correlate with actin cytoskeleton disruption, we selectively labeled presynaptic actin by neuronally expressing actin-RFP, which on its own did not obviously disrupt NMJ morphology or animal viability. At WT NMJs, actin-RFP localized to puncta that were distributed throughout boutons (Fig. 6*A*), disappeared and formed on a ~30-s timescale (Movie S1), and have been previously implicated in

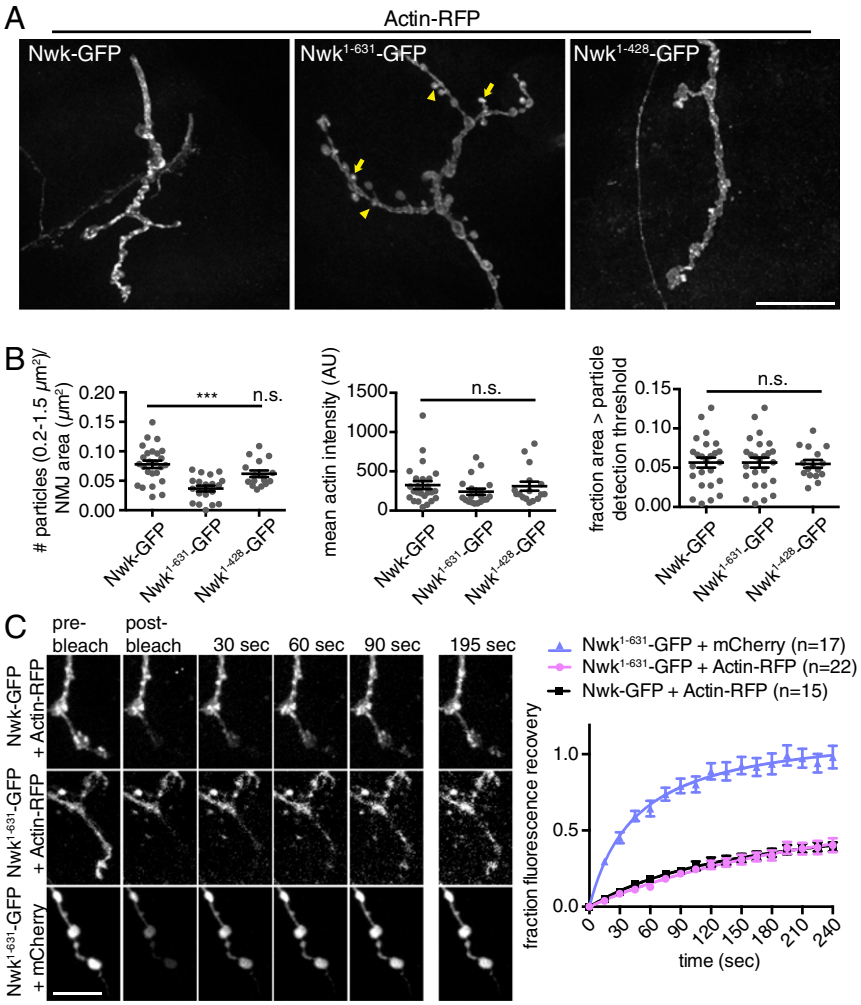

Fig. 6. Nwk autoinhibition is required for spatially controlled actin assembly. (*A*) Nwk$^{1–631}$-GFP causes mislocalization of actin-RFP from dynamic patches. Images show representative maximum intensity projections of confocal Z-stacks of NMJs on muscle 4, segments A2-A3. Arrows indicate large actin accumulations, and arrowheads indicate small puncta. (Scale bar: 20 μm.) (*B*) Quantification of particle size distribution, mean NMJ actin-RFP intensity, and fraction of NMJ area over the particle detection threshold (200% of the mean actin-RFP intensity). The genotype is elav^{C155}/Y; UAS-Nwk^{X}-GFP/+; UAS-actin-RFP/+, UAS-Nwk^{FL}-GFP n = 25 NMJs; UAS-Nwk$^{1–631}$-GFP n = 19 NMJs; UAS-Nwk$^{1–631}$-GFP n = 16 NMJs. Statistical significance was calculated by ANOVA followed by Tukey's pairwise test. (*C*) Actin-RFP exhibits polymer-like turnover despite its diffuse distribution. Images show representative maximum intensity projections of live confocal Z-stacks from NMJ FRAP experiments. (Scale bar: 10 μm.) (*D*) Quantification of FRAP data.

synaptic endocytosis (35). In stark contrast, the majority of actin-RFP was diffusely localized in Nwk$^{1–631}$-expressing NMJs, although it did accumulate in some very small or very large puncta (arrows and arrowheads in Fig. 6*A*). We quantified this difference in distribution by measuring the number of puncta 0.2–1.5 μm^2 in diameter, and found significantly fewer puncta in this intermediate size range per NMJ area in Nwk$^{1–631}$-expressing NMJs. The mean actin intensity and the number of pixels over our particle selection threshold were similar to those values seen in full-length Nwk-expressing NMJs, suggesting that the distribution, but not the amount, of actin-RFP is altered. Importantly, actin-RFP distribution was not altered in NMJs expressing only the F-BAR domain of Nwk (Nwk$^{1–428}$-GFP), suggesting that the redistribution of actin is Nwk SH3a domain-dependent.

The apparently diffuse distribution of actin-RFP in Nwk$^{1–631}$-expressing NMJs could reflect either unpolymerized actin or ectopic actin assembly throughout the NMJ. To distinguish between these possibilities, we used fluorescence recovery after photobleaching (FRAP) to measure the turnover rate of actin-RFP. Actin-RFP exhibited similar slow and incomplete recovery in NMJs expressing either full-length Nwk-GFP or Nwk$^{1–631}$-GFP, suggesting that its diffuse localization on deregulation of Nwk is due to ectopic polymerization rather than to a lack of polymerization (Fig. 6*C* and Movies S1 and S2). In contrast, the free fluorescent protein mCherry recovered completely (Fig. 6*C* and Movie S3). Thus, our results suggest that NMJ morphological defects on deregulation of Nwk correlate with spatially unregulated actin assembly.

Discussion

Here we report that the F-BAR protein Nwk exhibits autoinhibitory interactions between its SH3 and its F-BAR domains both in solution and on membranes. In addition to controlling membrane binding, these autoinhibitory interactions also, unexpectedly, inhibit SH3 domain-mediated WASp activation. Similarly, autoregulation is required in vivo to restrict SH3 domain-dependent synaptopod formation, synaptic growth, and actin organization at *Drosophila* NMJs. Thus, autoregulation of Nwk coordinates the intramolecular control of membrane binding with the intermolecular control of SH3 domain effectors such as WASp (Fig. 7).

A number of BAR and F-BAR proteins are regulated by autoinhibitory interactions, including endophilin (11, 36), Syndapin (8), Amphiphysin (9, 14), Cdc15 (37), IRSp53 (12), srGAP (13), and

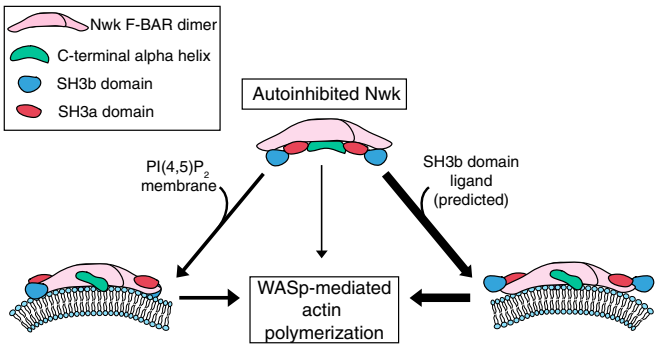

Fig. 7. Model for autoregulation of Nwk F-BAR and SH3 domains. Autoregulated Nwk is restricted from membrane binding and SH3a-mediated WASp activation, both in solution and on membranes. We hypothesize that release of SH3b-mediated autoinhibition coordinately promotes membrane association together with activation of SH3a domain effects on WASp or other ligands.

Nwk (16). Although structural information has been obtained for several of these autoinhibited proteins, it has been difficult to determine which conformations and interaction interfaces correspond to autoinhibited and/or membrane-bound states. By directly comparing single-particle EM structures for Nwk on carbon film and on membrane monolayers, we found that the SH3 domains shift from the concave surface to a lateral position on membrane binding. These multiple conformations may be a general feature of F-BAR domain autoregulation, and could explain some of the heterogeneity of F-BAR–SH3 domain orientations that has been observed in single structural snapshots (8). Furthermore, we found that the alpha-helical extension of the F-BAR domain is located near the membrane-binding concave surface of Nwk, and shifts to a position alongside the F-BAR domain on membrane binding. This structural shift also may apply to other F-BAR proteins, including SRGAP family members and Fes, which have similar C-terminal alpha helical regions that in some cases have been shown to be required for their membrane deformation activity (13).

Until now, the prevailing model has been that the SH3 domains bind and obstruct the concave membrane-interacting surface of the F-BAR domain, and that these interactions are released to allow membrane binding. Our structure of Nwk in solution supports one key aspect of this model, that the SH3 domains bind the concave surface of the F-BAR. In contrast, we found that in membrane-bound structures, the SH3 domains of Nwk are not completely disordered, but instead are on average maintained in positions on either side of the F-BAR domain. Nonetheless, our data cannot rule out the possibility of some heterogeneity in the positions of the SH3 domains in either solution or membrane-bound forms, representing some fraction of protein that exists in an opened or active conformation. We found that full-length Nwk and the Nwk F-BAR domain bind and deform membranes in a similar manner, and also organize into similar higher-order assemblies on membranes (Fig. S5) (16, 17). These data suggest that the continued association of SH3 domains in the membrane-bound state does not influence membrane remodeling. Instead, our in vitro and in vivo data support an alternative function for persistent SH3 domain association with the F-BAR; the F-BAR-SH3b domain association constrains SH3a domain activities both in solution and on membranes.

To date, there has been little consideration of how F-BAR–mediated autoregulatory interactions might govern SH3 domain activities. In Syndapin 1, the single autoregulatory SH3 domain contacts the F-BAR near the PxxP-binding groove, suggesting that proline-rich ligands (perhaps including WASp) could relieve autoinhibition. In fact, the dynamin proline-rich domain releases Synd autoinhibition of membrane remodeling in heterologous cells and in vitro (8). Furthermore, full-length Synd can effectively stimulate WASp (31), suggesting that autoinhibition does not affect WASp activation. Nwk appears to act by a different mechanism, perhaps owing to its second SH3 domain, which may have evolved to allow a more sophisticated mechanism of autoinhibition and release. This concept is supported by our in vivo data showing that loss of the second SH3 domain leads to gain-of-function effects. PIP_2-rich membranes exhibit only modest effects on the activity of Nwk on WASp, suggesting that binding to charged membranes is not sufficient for full release from autoinhibition. Indeed, in the cell, driving F-BAR binding by increasing membrane charge alone would not effectively couple the membrane-deforming and SH3 domain activities of Nwk, because Nwk deforms membranes only within a "sweet spot" of negative charge, and deformation is disfavored at very high charge (16). We also found that WASp only modestly increases lipid binding by autoregulated Nwk. Taken together, these results indicate that the SH3b domain autoinhibitory clamp persists even in the presence of SH3a domain proline-rich ligands and membranes, and are consistent with our structural data.

These results also suggest that an additional activation step may be required to release the SH3a domain for interaction with effectors. One possibility is that an additional F-BAR– or SH3b-interacting ligand releases Nwk from its autoinhibited state. Interestingly, interactions between the F-BAR domain of the murine Nwk homolog FCHSD1 and the SH3 domain of SNX9 are associated with enhanced activation of WASp in vitro (21), although it is not clear whether this is the result of release of FCHSD1 autoinhibition or FCHSD1 activation of SNX9–WASp interactions. Clearly, further work is needed to identify which of a growing number of Nwk ligands are involved in the release from autoinhibition, and how they accomplish this effect (19, 20, 23).

Finally, given this tight autoregulation of membrane binding and SH3 domain interactions, our data suggest that a significant fraction of Nwk in vivo may be in an inactive conformation. We generated a deregulated Nwk by deleting its critical autoregulatory SH3b domain and found that this protein exhibited unpredicted activity at the *Drosophila* NMJ: SH3a-dependent induction of synaptopods and new boutons. Importantly, the F-BAR domain alone was not sufficient to induce synaptopods, and the SH3b domain was required to inhibit their formation, providing strong in vivo evidence for autoinhibition of SH3a domain activities.

Until now, Nwk has been thought to only constrain (rather than promote) synaptic growth, by regulating the traffic of growth factor receptors (19, 20, 23). Our present results suggest that Nwk plays a previously unrecognized role, downstream of its function in constraining signaling, to drive membrane remodeling, synaptopod formation, and growth of new boutons. Consistent with a physiological role for Nwk in synaptopod formation, the cytoskeletal protein Hts/Adducin negatively regulates synaptopods at the *Drosophila* NMJ (34), and its homolog γ-Adducin was recently shown to interact with a mouse Nwk homolog (38). Synaptopods arise from a Nwk-SH3a domain-dependent activity on WASp or some other SH3a domain ligand. Pinpointing the role of WASp in Nwk-induced synaptopod formation will be challenging, given that WASp has critical, Nwk-independent roles in NMJ morphology both presynaptically and postsynaptically (39, 40). Thus, future work is required to determine precisely which pathways lie downstream of Nwk SH3a in synaptopod formation, and to identify the ligands that release SH3b-mediated autoinhibition in vivo.

In summary, our results provide four key insights into Nwk structure, regulation, and mechanism. First, they show that both membrane binding and WASp activation by Nwk are highly autoregulated in solution. Second, they reveal that autoregulation of SH3a-mediated activities persist even once Nwk is membrane-bound. Third, they imply that additional ligands of Nwk are critical for full release from autoinhibition. Fourth, they uncover potential previously unknown roles for Nwk in synaptic growth in vivo. Taken

together, these results suggest an unexpected level of coordination in the regulation of F-BAR membrane remodeling and SH3 effector binding, which has broad implications for understanding the control of other BAR proteins in a wide range of biological functions.

Materials and Methods

Protein Purification and Interaction Assays. N-terminally His-Xpress–tagged proteins were purified as described previously (16, 17). In brief, proteins were purified from BL21(DE3) *Escherichia coli* using cobalt columns, followed by ion exchange and gel filtration into 20 mM Tris pH 7.5, 50 mM KCl, 0.1 mM EDTA, and 0.5 mM DTT. WASp^{143} was purified as described previously (23). The Arp2/3 complex was purchased from Cytoskeleton, Inc. Coprecipitation assays with GST-tagged proteins were conducted as described previously (16). Pellets and supernatants were denatured in Laemmli sample buffer and fractionated by SDS/PAGE, followed by immunoblotting with α-WASp antibody P5E1 (41).

EM and Single-Particle Analysis. For single-particle EM on carbon film, 3 μL of 0.7 μM Nwk in 20 mM Hepes pH 7.5 and 100 mM NaCl were incubated for 30 s on glow-discharged carbon-coated copper grids (400 mesh; Ted Pella), and then negatively stained with 1% uranyl acetate. Samples were then imaged on an FEI Tecnai F30 transmission electron microscope, operating at 200 kV. Images were captured using an Eagle CCD (FEI) at 40,000× magnification and 1.5–1.9 μm underfocus.

For single-particle EM on lipid monolayers, 1 μL of 1 mg/mL lipids [molar percentages of PC/PE/PS/PI(4,5)P2: 65/15/10/10, with <0.1% rhodamine-PE for visualization, dissolved in 20:9:1 chloroform:methanol:water] was incubated on a 25-μL drop of buffer (20 mM Hepes pH 7.5, 100 mM NaCl) in a Teflon well in a humid chamber at 4 °C for 1 h, as described previously (17). Lipid monolayers were then lifted onto the carbon-coated grids, and the buffer was replaced with a solution containing 0.7 μM Nwk, followed by incubation for 30 min in a humid chamber. Images were recorded on a JEOL 2100 transmission electron microscope, operating at 200 kV at 0° and 45° tilt angles. Images were captured using an Ultrascan 1000XP CCD (Gatan) at 40,000× magnification.

To obtain a 3D reconstruction of Nwk$^{1–731}$ on carbon film, particles were selected from the EM images using Boxer (42) and windowed into 128 × 128 pixel images. These were then filtered and normalized to an SD of 2, and processed for reference-free classification in IMAGIC (43). Multivariate statistical analysis (24, 44) on aligned particles produced eigenimages (Fig. S3*A*) that suggest that particles have twofold symmetry. A total of 3,418 particles were categorized into 100 2D class averages. At this stage, 550 particles from class averages that were similar in shape to projections of the F-BAR domain alone were removed. These are likely to represent the fraction of membrane-free Nwk in an open conformation with poorly positioned SH3 domains, consistent with the ability of full-length Nwk to bind membranes, albeit at a much lower efficiency than the isolated Nwk F-BAR (16, 17). We used the angular reconstitution method (24) and the back-projection algorithm to obtain a first rough 3D model. The density map was then improved using the FREALIGN program (45). We calculated a 3D reconstruction without imposing twofold symmetry, confirming that the reconstruction still displayed quasi-twofold symmetry (Fig. S3*D*). Based on this observation, and the twofold symmetrical eigenimages, C2 symmetry was applied to the 3D reconstruction at the final stage.

To obtain a 3D reconstruction of Nwk$^{1–731}$ on membrane monolayers, particles were selected from the EM images using Boxer (42) and windowed into 128 × 128 pixel images. These were then filtered and normalized to an SD of 2. An initial 3D model of full-length Nwk on lipid monolayers was reconstructed from 647 pairs of particles from tilted images (0° and 45°) in EMAN2.1 software using the random conical tilt (RCT) method (42). This method is well suited for reconstruction from particles with a preferred orientation on the surface. In brief, untilted images were first corrected for contrast transfer function of the electron microscope, and then used for classification to obtain reference-free class averages. Although symmetry was not applied, most of the class averages were twofold symmetric. This was also supported by the production of eigenimages demonstrating the presence of twofold symmetrical particles (Fig. S6*A*). An initial 3D reconstruction containing all Nwk orientations was calculated without imposing symmetry, using the in-plane rotation angles determined by rotational alignment and the preselected tilt angle of 45° using the RCT method implemented in the processing package EMAN2.1.

For the second refinement, a larger dataset of 5,017 particles was analyzed with EMAN2.1. At this stage, particles from class averages with convex-down orientation were removed from the dataset; 4,050 concave-down and side-down oriented particles remained. The density map was then improved using the FREALIGN program (45). A 3D reconstruction was calculated without imposing twofold symmetry, confirming that the reconstruction still displayed quasi-twofold symmetry (Fig. S6*D*).

Based on this observation, and on the twofold symmetrical eigenimages, C2 symmetry was applied to the reconstruction at the final stage. Orientational distributions of Nwk were studied by projection matching. To identify side-lying Nwk$^{1–731}$ particles, class averages were selected with the highest correlation (R = 0.6–0.7) to the indicated reprojections of the 3D reconstruction (Fig. 1*B*), rotated along its long axis in 10° increments. All particles in class averages corresponding to that indicated orientation were pooled into a single class average. To orient Nwk$^{1–428}$ class averages (Fig. 1*C*), we similarly used a set of 20 reference projections, generated by rotating the predicted Nwk$^{1–313}$ Phyre structure (17) (filtered to 20 Å) along its long axis in 10° increments.

To generate unbiased difference maps, matching orientations of Nwk$^{1–428}$ and Nwk$^{1–731}$ were aligned using IMAGIC before subtraction. For comparing orientational distributions of Nwk$^{1–731}$ on carbon and on membranes, ~1,000 particles were collected at random from each sample and processed in IMAGIC. After classification of the particles, each class sum image was aligned against the Nwk$^{1–313}$ references. Each class was assigned to the orientation with the best cross-correlation coefficient obtained (Table S1).

To visualize differences between the full-length Nwk and its F-BAR domain, a low-pass (i.e., filtered to 20 Å) model of the Nwk F-BAR domain (17) and SH3b domain (16) was fitted into the 3D reconstruction in Chimera 1.9. We note that this homology was not used for calculating any of our 3D reconstructions, and is shown here for comparative purposes only.

Actin Polymerization Kinetics. Rabbit muscle actin [5% (mol/mol) pyrene-labeled] was gel-filtered, exchanged from Ca^{2+} to Mg^{2+}, and assembled at a final concentration of 2.5 μM as described previously (46). Proteins were preincubated with 10 μM liposomes or control buffer for 30 min before actin assembly reactions (Fig. 5). Assembly was monitored with a spectrofluorometer (Photon Technology International) using an excitation wavelength of 365 nm and an emission wavelength of 407 nm. Rates were calculated from slopes of curves in the linear range, and curves were plotted using GraphPad Prism software.

Lipid Interaction Assays. Lipid cosedimentation assays were conducted as described previously (17). In brief, liposomes were swelled from dried lipid films in 20 mM Hepes pH 7.5 and 100 mM NaCl. Specific lipid compositions are indicated in the figure legends. Proteins were then mixed with 1 mg/mL liposomes, incubated for 30 min at room temperature, and then pelleted for 20 min at 18,000 × *g* at 4 °C. Pellets and supernatants were then denatured in Laemmli sample buffer and fractionated by SDS/PAGE, followed by Coomassie staining.

***Drosophila* Genetics and NMJ Analyses.** Flies were cultured using standard media and techniques. UAS-Nwk constructs were generated using Gateway technology (Invitrogen) in pBI-UASC-eGFP (47), as described previously (16). These transgenes were injected into flies (Genetic Services or Rainbow Gene), using Φc381 recombinase at the Attp40 locus (48), to ensure that all constructs were in a similar genomic context. For rescue experiments, transgenes were crossed into the *nwk*^{2} mutant background and then crossed to *elav*^{C155}; *nwk*^{1} flies. UAS-actin5C-RFP (49) was obtained from the Bloomington Drosophila Stock Center.

For analysis of NMJ morphology and protein localization at the NMJ, flies were cultured at low density at 25 °C. Wandering third instar larvae were dissected in calcium-free HL3.1 saline (50) and fixed for 30 min in HL3.1 containing 4% formaldehyde before antibody staining. For analysis of NMJ morphology, NMJs on muscle 4, segments A2 A4 from male or female larvae were selected for analysis. NMJs were stained with Alexa Fluor 647-conjugated α-HRP (Jackson Immunoresearch) and α-Dlg or α-BRP primary antibodies (Developmental Studies Hybridoma Bank) with rhodamine red-X–conjugated secondary antibodies (Jackson Immunoresearch). For analysis of actin-RFP localization and turnover, NMJs on muscle 4, segments A2–A4 were selected for analysis from male larvae or the genotype *elav*^{C155}/Y; UAS-Nwk^{X}/+; UAS-actin-RFP/+/.

Spinning-disk confocal imaging was performed at room temperature with a Nikon Ni-E upright microscope equipped with 60× (NA 1.4) and 100× (NA 1.45) oil immersion objectives (for fixed sample imaging), a 100× (NA 1.1) water-dipping objective (for live imaging), a Yokogawa CSU-W1 spinning-disk head, and an Andor iXon 897U EMCCD camera. Laser scanning confocal imaging was conducted at room temperature on an Ni-E inverted microscope equipped with a Nikon C2 confocal head and a 60× (NA 1.4) objective. Images were collected using Nikon Elements AR software. For FRAP data acquisition, confocal Z-stacks (with 1-μm steps) were collected every 15 s for 5 min, with manual focus adjustment. Following acquisition of two or three initial Z-stacks to assess prebleach intensity, terminal boutons representing

<10% of the total NMJ area were photobleached using a 405-nm laser (50% power, 2 s), directed to an Andor Mosaic 3 digital micromirror device.

Fluorescence microscopy image analysis was performed in FIJI (51) on average-intensity 2D projections from confocal Z-stacks. Only type Ib innervation on muscle 4 was quantified. Thin NMJ protrusions lacking significant α-Dlg postsynaptic immunoreactivity were defined as synaptopods. Actin-RFP distribution was quantified within the presynaptic area defined by the Nwk-GFP signal. Background signal (defined from an adjacent area of muscle) was subtracted from the images, the mean NMJ RFP signal was calculated, and the image was thresholded at 200% of the mean NMJ signal. This threshold level served as an unbiased method to define actin-RFP particles. Particle numbers and sizes were then calculated from this thresholded image using the "Particle Analysis" function of FIJI. For FRAP analysis, XY drift was corrected automatically using the Stackreg rigid body plug-in (52), and photobleaching was corrected using the FIJI simple ratio "Bleach Correct" function. Mean fluorescence recovery was measured in the bleached area, normalized to prebleach (1) and postbleach (0) fluorescence intensities, and analyzed with GraphPad Prism.

Statistical Analyses. Statistical significance was calculated with GraphPad Prism software using Student's *t* test or ANOVA, followed by Tukey's pairwise test, with $*P < 0.05$, $**P < 0.01$, and $***P < 0.001$.

ACKNOWLEDGMENTS. We thank Sal Alioto, Bruce Goode, Jessica Henty-Ridilla, Gabriel Lander, Mike Rigney, Steve Del Signore, and Shiyu Wang for assistance and helpful discussions. Monoclonal antibodies were provided by the Developmental Studies Hybridoma Bank. Single-particle electron microscopy studies were performed at the User Facility Center for Electron Microscopy, Department of Biology, Moscow State University. This work was supported by the Russian Science Foundation (Grant 14-14-00234, to O.S.S.), a Pew Scholar Award (to A.A.R.), an NIH/National Institutes of General Medical Sciences genetics training grant (T32 GM007122, to C.F.K.), a Howard Hughes Medical Institute Science Education grant (52008141, to S.A.W.), and a grant from the Brandeis Center for Bioinspired Soft Materials, a National Science Foundation Materials Research Science and Engineering Center (DMR-1420382).

1. McMahon HT, Boucrot E (2015) Membrane curvature at a glance. *J Cell Sci* 128(6): 1065–1070.
2. Owen DJ, et al. (1998) Crystal structure of the amphiphysin-2 SH3 domain and its role in the prevention of dynamin ring formation. *EMBO J* 17(18):5273–5285.
3. Takei K, Slepnev VI, Haucke V, De Camilli P (1999) Functional partnership between amphiphysin and dynamin in clathrin-mediated endocytosis. *Nat Cell Biol* 1(1):33–39.
4. Itoh T, et al. (2005) Dynamin and the actin cytoskeleton cooperatively regulate plasma membrane invagination by BAR and F-BAR proteins. *Dev Cell* 9(6):791–804.
5. Neumann S, Schmid SL (2013) Dual role of BAR domain-containing proteins in regulating vesicle release catalyzed by the GTPase, dynamin-2. *J Biol Chem* 288(35): 25119–25128.
6. Rotty JD, Wu C, Bear JE (2013) New insights into the regulation and cellular functions of the ARP2/3 complex. *Nat Rev Mol Cell Biol* 14(1):7–12.
7. Wang Q, et al. (2009) Molecular mechanism of membrane constriction and tubulation mediated by the F-BAR protein Pacsin/Syndapin. *Proc Natl Acad Sci USA* 106(31): 12700–12705.
8. Rao Y, et al. (2010) Molecular basis for SH3 domain regulation of F-BAR-mediated membrane deformation. *Proc Natl Acad Sci USA* 107(18):8213–8218.
9. Meinecke M, et al. (2013) Cooperative recruitment of dynamin and BIN/amphiphysin/Rvs (BAR) domain-containing proteins leads to GTP-dependent membrane scission. *J Biol Chem* 288(9):6651–6661.
10. Vázquez FX, Unger VM, Voth GA (2013) Autoinhibition of endophilin in solution via interdomain interactions. *Biophys J* 104(2):396–403.
11. Chen Z, et al. (2014) Intradimer/intermolecular interactions suggest autoinhibition mechanism in endophilin A1. *J Am Chem Soc* 136(12):4557–4564.
12. Kast DJ, et al. (2014) Mechanism of IRSp53 inhibition and combinatorial activation by Cdc42 and downstream effectors. *Nat Struct Mol Biol* 21(4):413–422.
13. Guerrier S, et al. (2009) The F-BAR domain of srGAP2 induces membrane protrusions required for neuronal migration and morphogenesis. *Cell* 138(5):990–1004.
14. Wu T, Baumgart T (2014) BIN1 membrane curvature sensing and generation show autoinhibition regulated by downstream ligands and PI(4,5)P2. *Biochemistry* 53(46): 7297–7309.
15. Guez-Haddad J, et al. (2015) The neuronal migration factor srGAP2 achieves specificity in ligand binding through a two-component molecular mechanism. *Structure* 23(11):1989–2000.
16. Kelley CF, et al. (2015) Membrane charge directs the outcome of F-BAR domain lipid binding and autoregulation. *Cell Reports* 13(11):2597–2609.
17. Becalska AN, et al. (2013) Formation of membrane ridges and scallops by the F-BAR protein Nervous Wreck. *Mol Biol Cell* 24(15):2406–2418.
18. Coyle IP, et al. (2004) Nervous wreck, an SH3 adaptor protein that interacts with Wsp, regulates synaptic growth in *Drosophila*. *Neuron* 41(4):521–534.
19. O'Connor-Giles KM, Ho LL, Ganetzky B (2008) Nervous wreck interacts with thickveins and the endocytic machinery to attenuate retrograde BMP signaling during synaptic growth. *Neuron* 58(4):507–518.
20. Rodal AA, et al. (2011) A presynaptic endosomal trafficking pathway controls synaptic growth signaling. *J Cell Biol* 193(1):201–217.
21. Cao H, et al. (2013) FCHSD1 and FCHSD2 are expressed in hair cell stereocilia and cuticular plate and regulate actin polymerization in vitro. *PLoS One* 8(2):e56516.
22. Sun X, et al. (2015) Transcription factor Sp4 regulates expression of nervous wreck 2 to control NMDAR1 levels and dendrite patterning. *Dev Neurobiol* 75(1):93–108.
23. Rodal AA, Motola-Barnes RN, Littleton JT (2008) Nervous wreck and Cdc42 cooperate to regulate endocytic actin assembly during synaptic growth. *J Neurosci* 28(33): 8316–8325.
24. Van Heel M (1987) Angular reconstitution: A posteriori assignment of projection directions for 3D reconstruction. *Ultramicroscopy* 21(2):111–123.
25. Frost A, et al. (2008) Structural basis of membrane invagination by F-BAR domains. *Cell* 132(5):807–817.
26. Padrick SB, et al. (2008) Hierarchical regulation of WASP/WAVE proteins. *Mol Cell* 32(3):426–438.
27. Rohatgi R, Ho HY, Kirschner MW (2000) Mechanism of N-WASP activation by CDC42 and phosphatidylinositol 4, 5-bisphosphate. *J Cell Biol* 150(6):1299–1310.
28. Prehoda KE, Scott JA, Mullins RD, Lim WA (2000) Integration of multiple signals through cooperative regulation of the N-WASP-Arp2/3 complex. *Science* 290(5492): 801–806.
29. Yarar D, Surka MC, Leonard MC, Schmid SL (2008) SNX9 activities are regulated by multiple phosphoinositides through both PX and BAR domains. *Traffic* 9(1):133–146.
30. Takano K, Toyooka K, Suetsugu S (2008) EFC/F-BAR proteins and the N-WASP-WIP complex induce membrane curvature-dependent actin polymerization. *EMBO J* 27(21):2817–2828.
31. Dharmalingam E, et al. (2009) F-BAR proteins of the syndapin family shape the plasma membrane and are crucial for neuromorphogenesis. *J Neurosci* 29(42):13315–13327.
32. Ataman B, et al. (2008) Rapid activity-dependent modifications in synaptic structure and function require bidirectional Wnt signaling. *Neuron* 57(5):705–718.
33. Piccioli ZD, Littleton JT (2014) Retrograde BMP signaling modulates rapid activity-dependent synaptic growth via presynaptic LIM kinase regulation of cofilin. *J Neurosci* 34(12):4371–4381.
34. Pielage J, Bulat V, Zuchero JB, Fetter RD, Davis GW (2011) Hts/Adducin controls synaptic elaboration and elimination. *Neuron* 69(6):1114–1131.
35. Zhao L, Wang D, Wang Q, Rodal AA, Zhang YQ (2013) *Drosophila* cyfip regulates synaptic development and endocytosis by suppressing filamentous actin assembly. *PLoS Genet* 9(4):e1003450.
36. Wang Q, Kaan HY, Hooda RN, Goh SL, Sondermann H (2008) Structure and plasticity of Endophilin and Sorting Nexin 9. *Structure* 16(10):1574–1587.
37. Roberts-Galbraith RH, et al. (2010) Dephosphorylation of F-BAR protein Cdc15 modulates its conformation and stimulates its scaffolding activity at the cell division site. *Mol Cell* 39(1):86–99.
38. Ukken FP, et al. (2016) BAR-SH3 sorting nexins are conserved interacting proteins of Nervous wreck that organize synapses and promote neurotransmission. *J Cell Sci* 129(1):166–177.
39. Khuong TM, Habets RL, Slabbaert JR, Verstreken P (2010) WASP is activated by phosphatidylinositol-4,5-bisphosphate to restrict synapse growth in a pathway parallel to bone morphogenetic protein signaling. *Proc Natl Acad Sci USA* 107(40): 17379–17384.
40. Nahm M, et al. (2010) dCIP4 (*Drosophila* Cdc42-interacting protein 4) restrains synaptic growth by inhibiting the secretion of the retrograde Glass bottom boat signal. *J Neurosci* 30(24):8138–8150.
41. Rodriguez-Mesa E, Abreu-Blanco MT, Rosales-Nieves AE, Parkhurst SM (2012) Developmental expression of *Drosophila* Wiskott-Aldrich syndrome family proteins. *Dev Dyn* 241(3):608–626.
42. Ludtke SJ, Baldwin PR, Chiu W (1999) EMAN: Semiautomated software for high-resolution single-particle reconstructions. *J Struct Biol* 128(1):82–97.
43. van Heel M, Harauz G, Orlova EV, Schmidt R, Schatz M (1996) A new generation of the IMAGIC image processing system. *J Struct Biol* 116(1):17–24.
44. van Heel M, Frank J (1981) Use of multivariate statistics in analysing the images of biological macromolecules. *Ultramicroscopy* 6(2):187–194.
45. Grigorieff N (2007) FREALIGN: High-resolution refinement of single particle structures. *J Struct Biol* 157(1):117–125.
46. Moseley JB, Maiti S, Goode BL (2006) Formin proteins: Purification and measurement of effects on actin assembly. *Methods Enzymol* 406:215–234.
47. Wang JW, Brent JR, Tomlinson A, Shneider NA, McCabe BD (2011) The ALS-associated proteins FUS and TDP-43 function together to affect *Drosophila* locomotion and life span. *J Clin Invest* 121(10):4118–4126.
48. Ni JQ, et al. (2008) Vector and parameters for targeted transgenic RNA interference in *Drosophila melanogaster*. *Nat Methods* 5(1):49–51.
49. Liu R, et al. (2008) Sisyphus, the *Drosophila* myosin XV homolog, traffics within filopodia transporting key sensory and adhesion cargos. *Development* 135(1):53–63.
50. Feng Y, Ueda A, Wu CF (2004) A modified minimal hemolymph-like solution, HL3.1, for physiological recordings at the neuromuscular junctions of normal and mutant *Drosophila* larvae. *J Neurogenet* 18(2):377–402.
51. Schindelin J, et al. (2012) Fiji: An open-source platform for biological-image analysis. *Nat Methods* 9(7):676–682.
52. Thévenaz P, Ruttimann UE, Unser M (1998) A pyramid approach to subpixel registration based on intensity. *IEEE Trans Image Process* 7(1):27–41.

Supporting Information

Stanishneva-Konovalova et al. 10.1073/pnas.1524412113

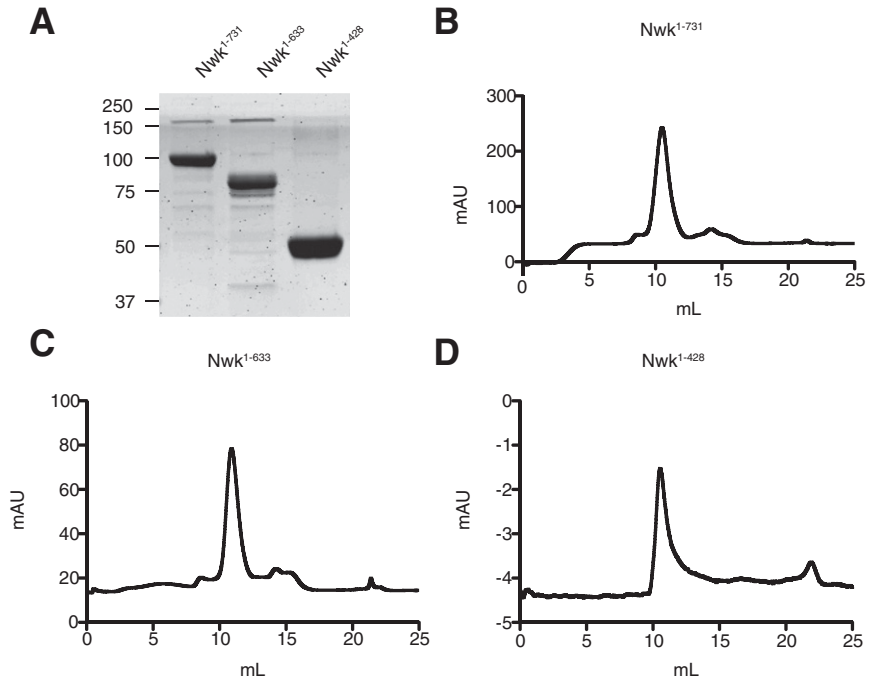

Fig. S1. Purified proteins used for EM studies. (*A*) Coomassie-stained SDS/PAGE gel showing purified proteins. (*B* and *C*) Gel filtration profiles from final step of Nwk$^{1–731}$ or Nwk$^{1–633}$ protein purification on an S200 column (GE Healthcare). (*D*) Gel filtration of Nwk$^{1–428}$ postpurifcation on a Superose 12 column (GE Healthcare).

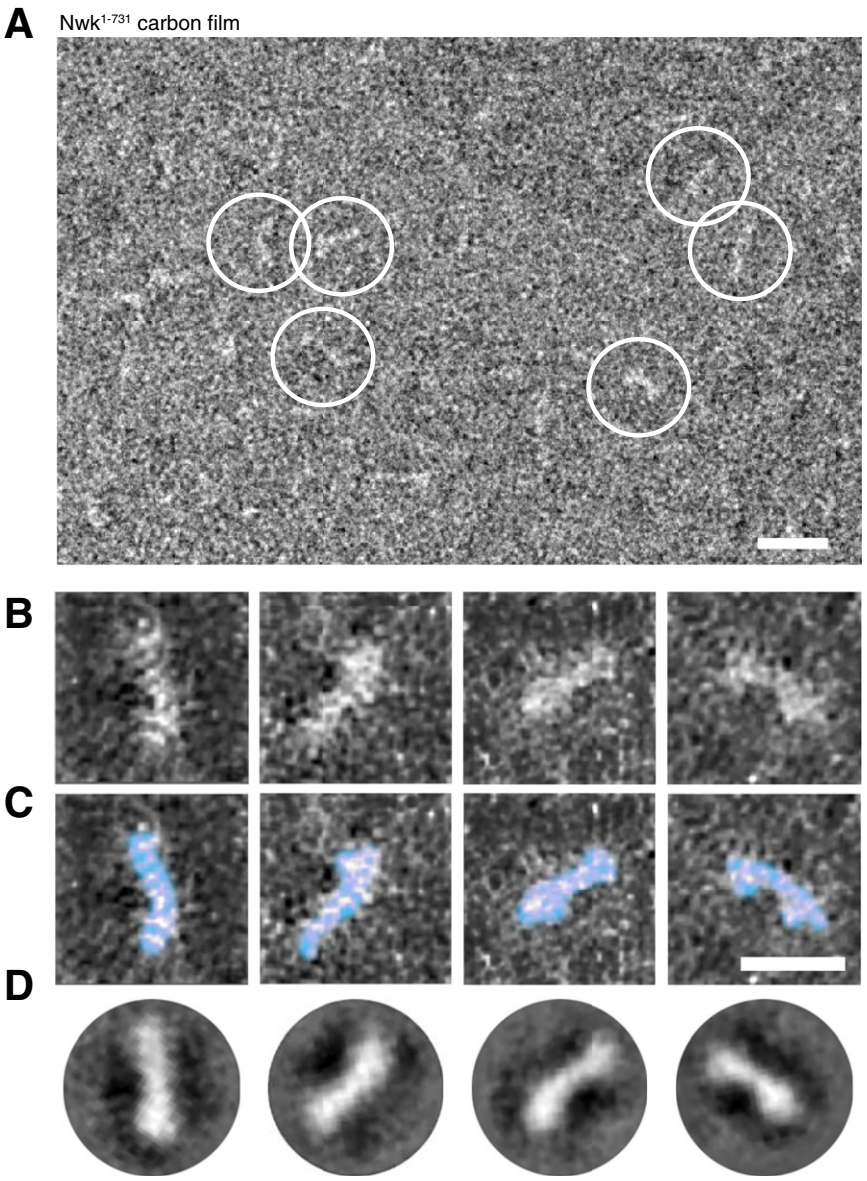

Fig. S2. EM of Nwk$^{1–731}$ on carbon film. (*A*) Electron micrograph of a field of Nwk$^{1–731}$ particles on carbon film. Open circles indicate single particles. (*B*) Gallery of representative single particles. (*C*) Same particles as in *B*, highlighted for clarity. (*D*) Some class averages from the initial classification, matching orientations of the single particles above. All EM images represent view from above the plane of the carbon film. (Scale bar: 20 nm.)

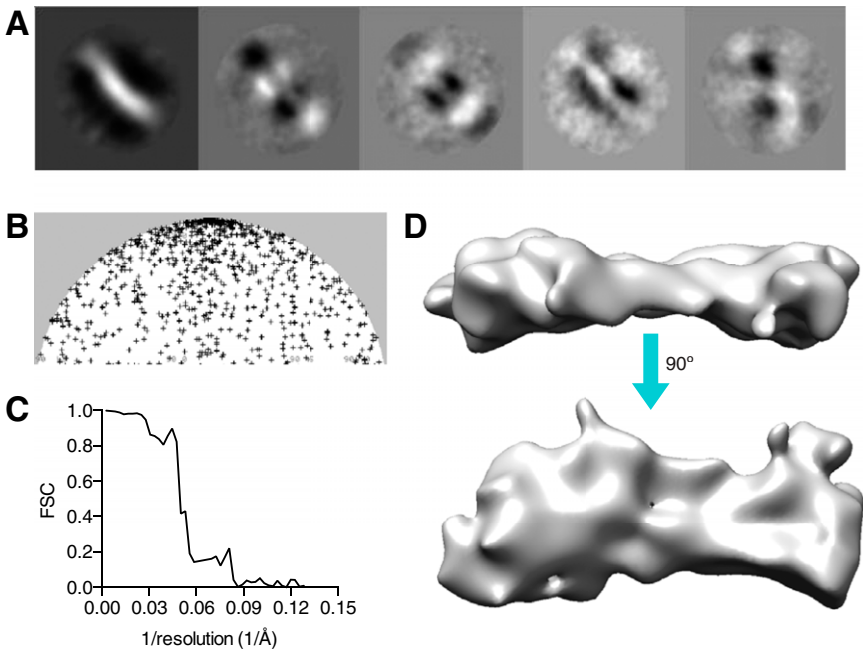

Fig. S3. A 3D reconstruction of Nwk$^{1–731}$ on carbon film. (*A*) Eigen images showing the twofold symmetry in the datasets. (*B*) Euler angles for Nwk$^{1–731}$ dimers on carbon film, showing well-distributed orientations. Each spot represents an orientation of the two Euler angles, Φ and θ. (*C*) Fourier shell correlation for Nwk$^{1–731}$ on carbon film. (*D*) 3D reconstruction of Nwk$^{1–731}$ before applying C2 symmetry.

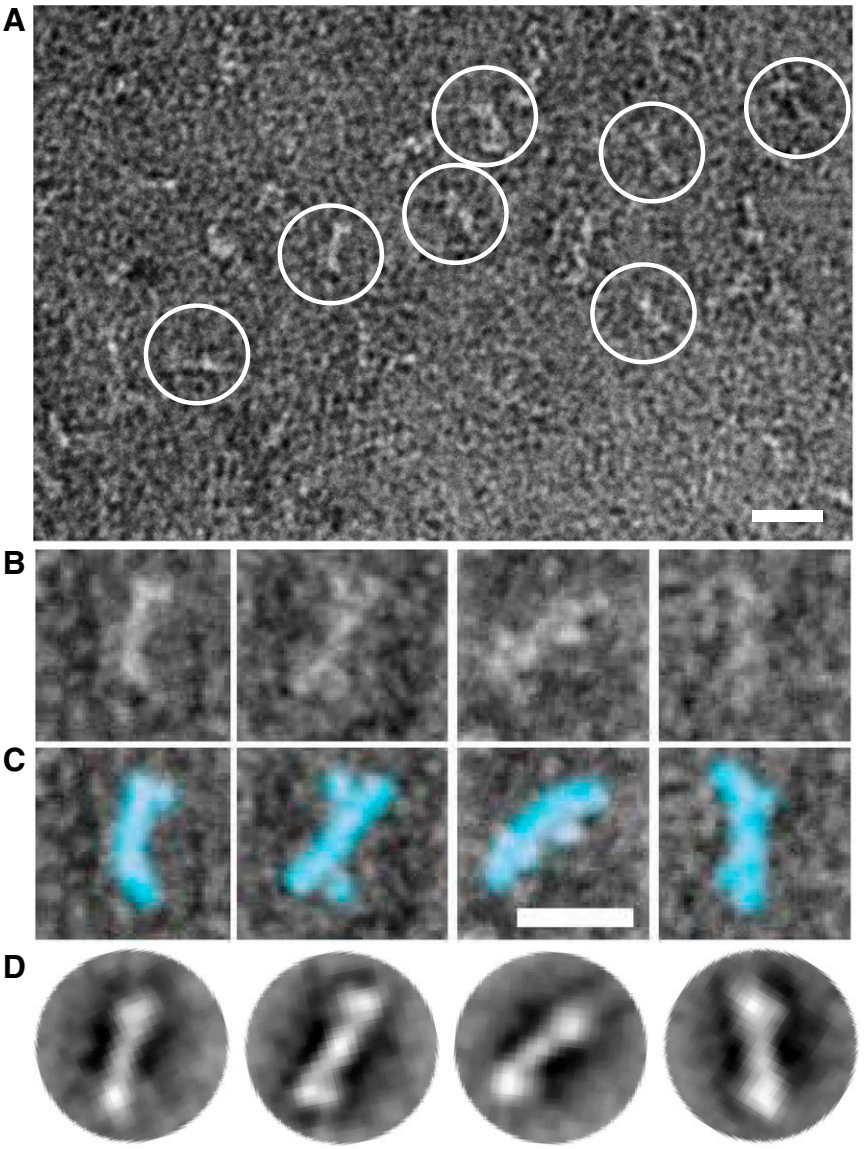

Fig. S4. EM of Nwk$^{1–731}$ on membrane monolayers. (*A*) Electron micrograph of a field of Nwk$^{1–731}$ particles on a lipid monolayer [molar percentages of PC/PE/PS/PI(4,5)P2: 65/15/10/10, with <0.1% rhodamine-PE for visualization]. Open circles indicate single particles. (*B*) Gallery of representative single particles. (*C*) The same particles as in *B*, highlighted for clarity. (*D*) Some class averages from initial classification, matching orientations of the single particles above. All EM images represent view from above the plane of the lipid monolayer. (Scale bars: 20 nm.)

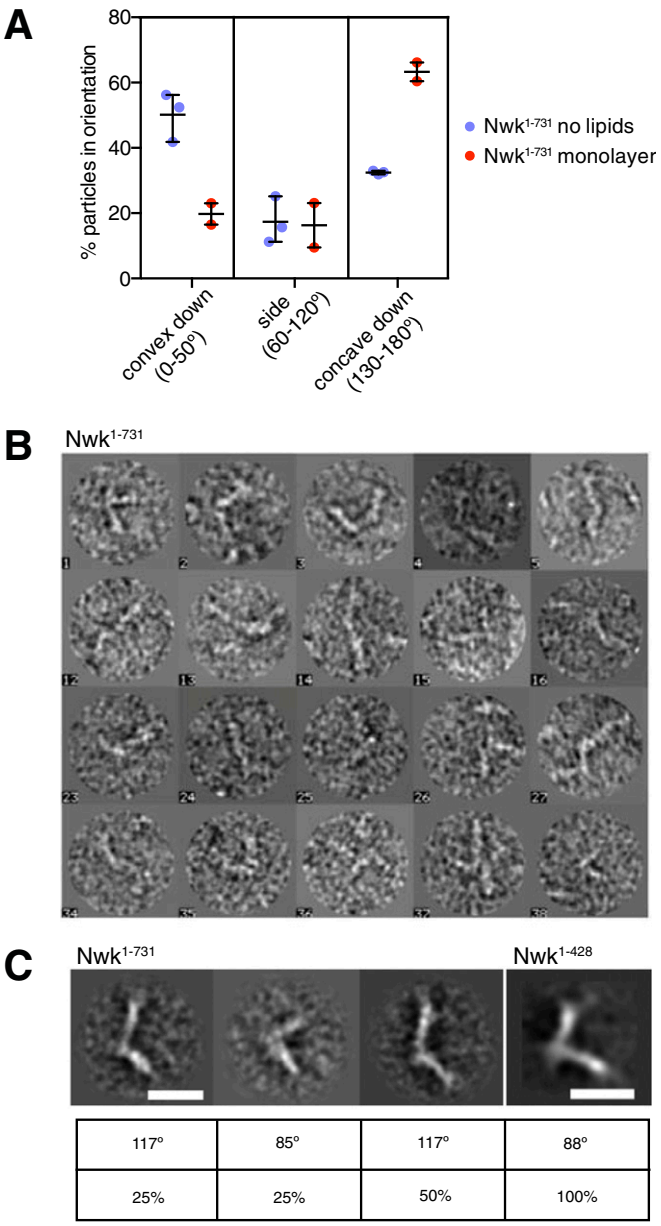

Fig. S5. Orientation and higher-order organization of Nwk on membrane monolayers. (*A*) Comparison of the orientation of Nwk$^{1–731}$ on carbon film and lipid monolayers. Orientations were assigned by calculating correlation coefficients (Table S1) to 2D projections of the 20 Å-filtered predicted structure of Nwk$^{1–313}$, rotated by 10° angles around its long axis. Bars represent mean distribution and range from two or three independent EM grids. (*B*) Selected zigzag associations between pairs of Nwk$^{1–731}$ dimers. (*C*) Class averages of Nwk$^{1–731}$ dimers (n = 114 particles) within zigzags, with Nwk$^{1–428}$ shown on the right for comparison (n = 263 particles) (17). The angle between dimers in each class is shown below in degrees; the fraction of single particles in each class is shown as a percentage. All EM images represent a view from above the plane of the membrane. (Scale bars: 20 nm.)

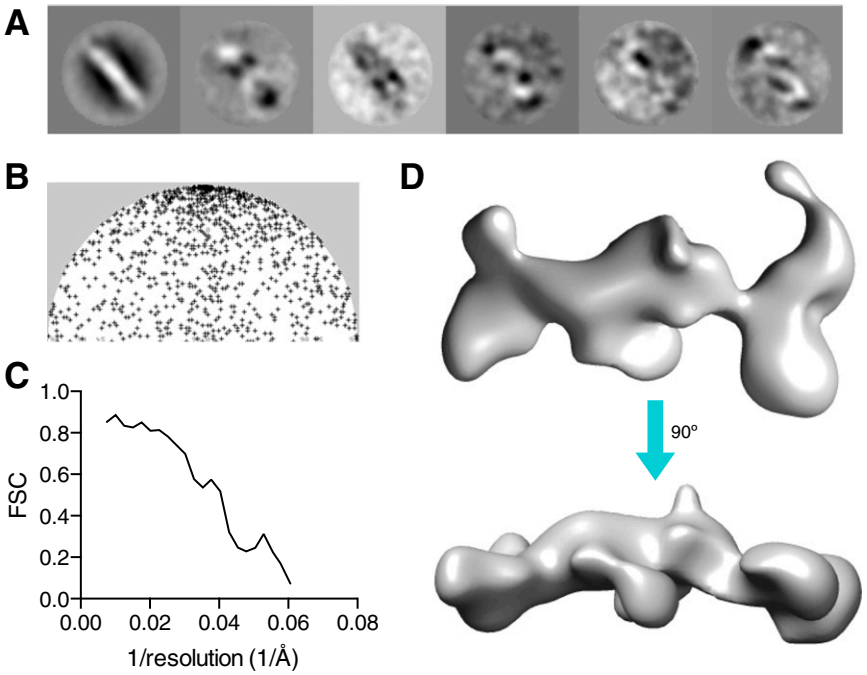

Fig. S6. A 3D reconstruction of Nwk$^{1–731}$ on membrane monolayers. (*A*) Eigen images showing the twofold symmetry in the datasets. (*B*) Euler angles for Nwk$^{1–731}$ on lipid monolayers. Note the presence of the preferred orientation of particles on the monolayer. (*C*) Fourier shell correlation for Nwk$^{1–731}$ on lipid monolayers. (*D*) 3D reconstruction of Nwk$^{1–731}$ on a lipid monolayer before applying C2 symmetry.

Table S1. Quantification of Nwk$^{1–731}$ orientations on carbon film or on membrane monolayers by EM and single-particle analysis, corresponding to Figs. S3 and S6

		Nwk$^{1–731}$, no membrane			10% PIP_2 monolayer	
Orientation	Degree of rotation	Grid A	Grid B	Grid C	Grid A	Grid B
Convex down	0	241	694	166	52	
	10	69	53	146	112	32
	20	131			75	49
	30	53	174	76		
	40	51				37
	50				74	
No. of particles		545	921	388	313	118
Percentage of particles		41.86	56.23	52.43	23.03	16.50
Side down	60	88		70		
	70				62	
	80	77	113			
	90		71			
	100	110				
	110			46		31
	120	53			67	134
No. of particles		328	184	116	129	165
Percentage of particles		25.19	11.23	15.68	9.49	23.08
Concave down	130	212		94	66	
	140				205	226
	150			40	223	
	160	151		102	142	138
	170	66	267		135	68
	180		266		128	
No. of particles		429	533	236	899	432
Percentage of particles		32.95	32.54	31.89	66.15	60.42
R range		0.5–0.8	0.6	0.6–0.8	0.6–0.74	0.7
Total particles		1,302	1,638	740	1,359	715

Datasets represent independently prepared EM grids. Particles were sorted into class averages and compared with 2D projections of the predicted Nwk$^{1–313}$ structure rotated around its long axis in 10° increments, and filtered to 20 Å (17). Class averages were assigned to the orientation with the highest R value. R value ranges for each data set are shown.

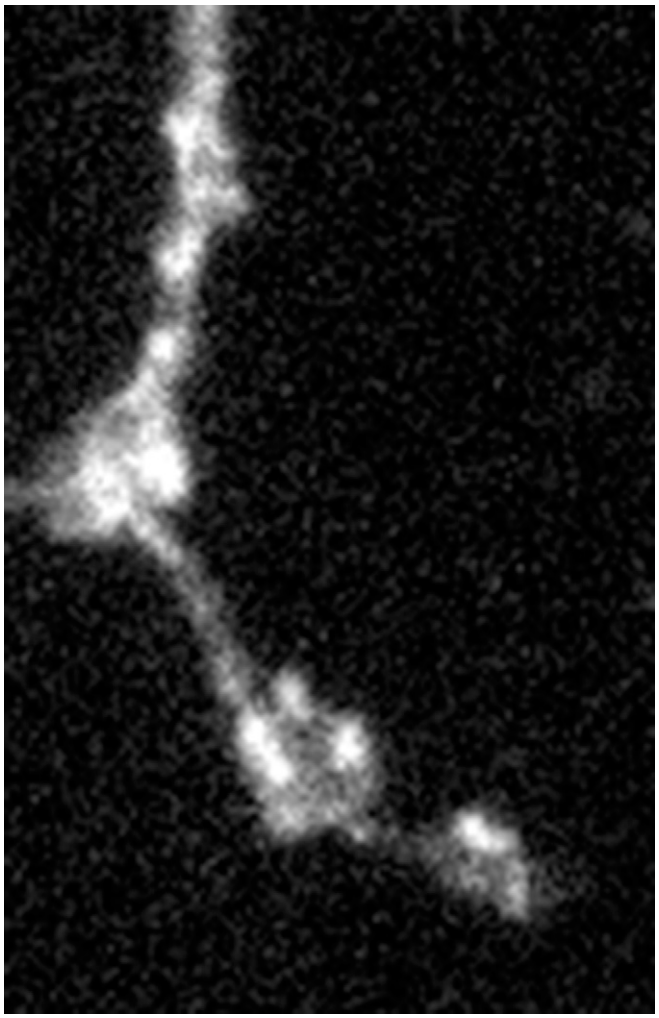

Movie S1. FRAP of actin-RFP at Nwk-GFP–expressing NMJs. The movie shows a 2D projection of a representative confocal stack time series. Time starts at the first frame after photobleaching frame. Images were collected every 15 s, and the movie is shown at 75× live speed. (Scale bar: 5 μm.)

Movie S1

Movie S2. FRAP of actin-RFP at Nwk$^{1–631}$-GFP–expressing NMJs. The movie shows a 2D projection of a representative confocal stack time series. Time starts at the first frame after photobleaching. Images were collected every 15 s, and the movie is shown at 75× live speed. (Scale bar: 5 μm.)

Movie S2

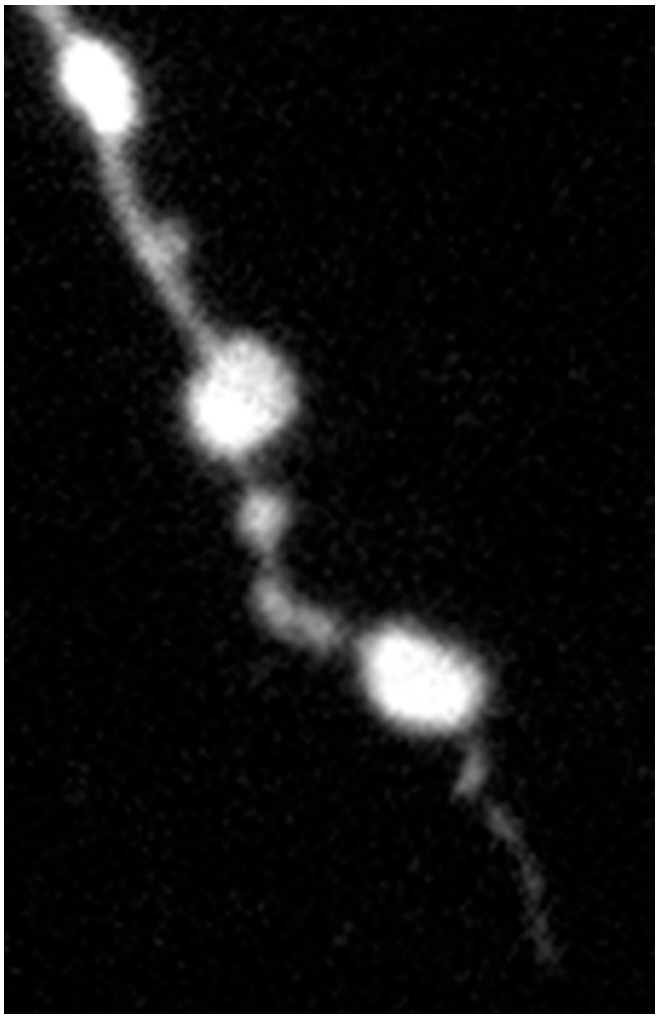

Movie S3. FRAP of mCherry at Nwk$^{1–631}$-GFP–expressing NMJs. The movie shows a 2D projection of a representative confocal stack time series. Time starts at the first frame after photobleaching. Images were collected every 15 s, and the movie is shown at 75× live speed. (Scale bar: 5 μm.)

Movie S3